

Enhanced α - γ Discrimination in Co-doped $\text{LaBr}_3\text{:Ce}$

Kan Yang, *Member, IEEE*, Peter R. Menge, *Member, IEEE*, and Vladimir Ouspenski

Abstract— $\text{LaBr}_3\text{:Ce}$ crystal scintillator can be co-doped with various alkaline earth metals to improve light output and energy resolution of the basic scintillator. Another benefit is improvement of alpha/gamma discrimination via pulse shape analysis. $\text{LaBr}_3\text{:Ce}$ contains a low level of actinium contamination, which produces an alpha particle background in radiation energy spectra. This background is difficult to discriminate from gamma rays. Conversely, the addition of co-dopant into the crystal makes the alpha response much easier to distinguish. $\text{LaBr}_3\text{:Ce}$, Sr, for example, produces a slow decay component in the scintillation pulse when excited by radiation. The amplitude of the slow decay component changes in response to a gamma ray versus a heavy charged particle. The change in pulse shape can be used to eliminate the alpha background or enable detection of neutron reaction products.

Index Terms— Co-doping, LaBr_3 , neutron detection, pulse shape discrimination, radiation detection, scintillation.

I. INTRODUCTION

A SCINTILLATION radiation detector is more useful when it can distinguish between different types of incoming radiation such as gamma rays and alpha particles. $\text{LaBr}_3\text{:Ce}$ crystal is one of the best scintillators available for the detection of gamma rays. It has high light yield and excellent energy resolution [1]. However, it has poor ability to distinguish between gamma rays and heavy charged particles, such as alphas [2].

Much current study is underway on co-doped $\text{LaBr}_3\text{:Ce}$ to improve properties such as light output and energy resolution. Co-doping with small concentrations of strontium and other aliovalent elements has shown to improve light output by 30% and reduce the energy resolution to as low as 2.0% (FWHM at 662 keV) [3], [4]. The improvement in light output, energy resolution, and non-proportionality has been ascribed to increased shallow electron trapping due to the formation of $\text{Sr}_{\text{La}} - \text{V}_{\text{Br}}$ traps in Sr co-doped LaBr_3 [5], [6]. The additional electron traps reduce the free electron density at the initial thermalization stage of scintillation and prevent the free electrons from being quenched by the Auger mechanism [5], [6]. Ca or Sr co-doped $\text{LaBr}_3\text{:Ce}$ also produces a slow decay component in the scintillation pulse when excited by radiation. The slow decay component can be ascribed to the detrapping of electrons from the aforementioned traps [5]–[7].

Manuscript received June 12, 2015; revised September 26, 2015, November 20, 2015, and December 10, 2015; accepted January 01, 2016. Date of current version February 16, 2016.

K. Yang and P. R. Menge are with the Saint-Gobain Crystals, Hiram, OH 44234 USA (e-mail: kan.yang@saint-gobain.com).

V. Ouspenski is with the Saint-Gobain Recherche, 93303 Aubervilliers, France.

Color versions of one or more of the figures in this paper are available online at <http://ieeexplore.ieee.org>.

Digital Object Identifier 10.1109/TNS.2016.2515024

TABLE I
 LaBr_3 CRYSTALS TESTED

| Co-doping* | Relative Light Output | Energy Resolution @ 662 keV |
|------------------------|-----------------------|-----------------------------|
| Ce^{3+} only | 100% | 3.2% |
| 0.50% Ca^{2+} | 135% | 2.9% |
| 0.50% Sr^{2+} | 128% | 2.8% |

* at.% in the melt, with respect to La^{3+}

In this study, another use for co-doping in $\text{LaBr}_3\text{:Ce}$ has been discovered. Co-doping enhances discrimination between gamma rays and heavy charged particles via pulse shape analysis.

$\text{LaBr}_3\text{:Ce}$ contains a low level of actinium contamination [8], which produces an intrinsic alpha particle background at the rate of $0.2 - 0.8 \text{ Bq/cm}^3$. This background is difficult to separate from a gamma ray energy spectrum using standard $\text{LaBr}_3\text{:Ce}$. However, the addition of a small amount of co-dopant into the crystal makes the alpha response much easier to distinguish using pulse shape discrimination. This slow decay component contains less of the total light pulse when the radiation is a heavy charged particle versus a gamma ray (or an electron). The intrinsic alpha particle background can be removed from gamma ray spectra by comparing the magnitude of the slow decay components.

Furthermore, thermal neutron detection and discrimination with $\text{LaBr}_3\text{:Ce}$ co-dopant is now possible. If the crystal is placed in proximity to a neutron reactive material such as ^6LiF or $^{10}\text{B}_4\text{C}$, a dual neutron/gamma ray detector can be constructed. These neutron reactive materials produce heavy charged particles following neutron absorption. Transport of these particles into LaBr_3 creates a signal that is distinguishable from gamma rays.

II. EXPERIMENTAL SETUP

Three $01'' \times 1''$ LaBr_3 crystals studied in this research were grown by Saint-Gobain Crystals. All crystals were doped with 5% Ce in the melt. The crystals were wrapped with Teflon reflector and hermetically packaged in titanium housings with sapphire optical windows on one end. Each crystal was optically coupled to the sapphire window by a clear silicone rubber. Table I shows the crystal compositions and scintillation properties of packaged crystals.

For pulse height spectra measurements, the samples were coupled to an Electron Tubes 9305 photomultiplier tube (PMT) with a modified voltage divider [9] with linear response at high energies. Background spectra were acquired for each sample for 24 h.

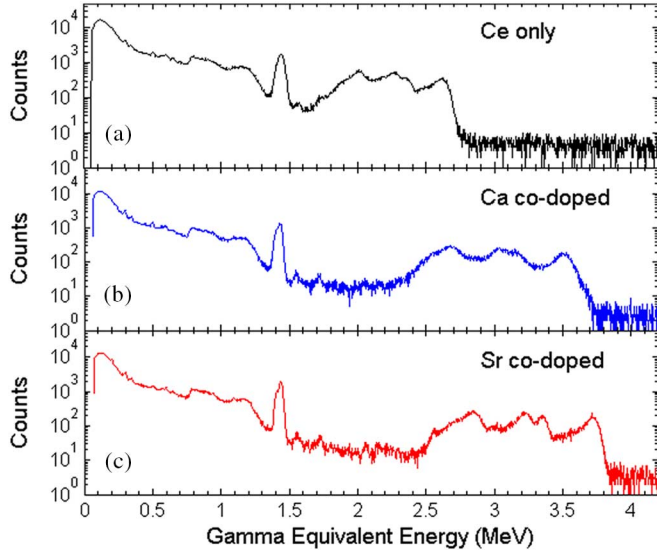


Fig. 1. Pulse height spectra of radiation background for Ce only and co-doped $\text{LaBr}_3:\text{Ce}$ samples. The gamma equivalent energy of alpha particles is increased with co-doping.

For pulse shape analysis, the packaged detectors were coupled to a Photonis XP2020Q PMT by optical grease. PMT anode signals were recorded by a CAEN DT5751 1-GHz desktop digitizer for post measurement analysis.

For neutron measurements, we surrounded an Sr^{2+} co-doped crystal with ^6LiF powder and coupled to the same Photonis XP2020Q PMT by optical grease. ^{252}Cf (35 ng) was used as the neutron source. The detector was placed approximately 8" from the ^{252}Cf source. The source was surrounded by a shell of 0.25" thick Pb to attenuate the gammas. High density polyethylene (HDPE) of 5" thickness was placed between the source and the detector to moderate the neutrons.

III. RESULTS AND DISCUSSIONS

A. Radiation Background in Co-doped LaBr_3

The internal radiation background in LaBr_3 comes from two major sources. First is the naturally occurring radiative isotope ^{138}La with 0.090% natural abundance. ^{138}La decays through either electron capture or β^- decay and emits two γ rays at 1435.8 keV and 788.7 keV. A coincident electron is also emitted with the 788.7 keV gamma ray forming the beta continuum [10]. The 1435.8 keV gamma ray often coincides with the ^{138}Ba K x-ray forming a peak near 1468 keV [11], [12]. A lower energy peak near 1440 keV is formed by the 1435.8 keV gamma coinciding with the L and M cascade x-rays [12]. The second source for internal radiation comes from the ^{227}Ac contamination in La. ^{227}Ac and many of its daughter particles undergo α decay and emit α particles with energies ranging from 5.042 MeV to 7.386 MeV [8], [11]. Many of them have similar energies and cannot be clearly resolved by the pulse height measurement. X-rays and γ -rays are also produced by the ^{227}Ac decay chain. Since their energies are lower than 1.3 MeV [13], the corresponding photo-peaks reside inside the Compton + beta continuum produced by ^{138}La and are difficult to resolve.

As is shown in the energy spectrum in Fig. 1(a), the counts in the region below 1.5 MeV are mostly from the internal γ

and β from ^{138}La . The counts between approximately 1.7 and 2.7 MeV are from the α particles from ^{227}Ac decay chain.

The concentration of co-dopants (Ca and Sr) in the matrix is low (0.5 at% in the melt) and neither co-dopant has naturally occurring radioisotopes. Thus, the physical nature of radiation background of co-doped crystals should be the same as that of Ce only LaBr_3 . However, the background pulse height spectra of co-doped $\text{LaBr}_3:\text{Ce}$ are found to be significantly different from that of Ce only LaBr_3 . As is shown in Fig. 1(b) and (c), the gamma equivalent energies (GEE) of the ^{227}Ac alpha peaks are increased significantly by Ca or Sr co-doping. While the alpha counts appear at 1.7–2.7 MeV in $\text{LaBr}_3:\text{Ce}$, they appear at 2.3–3.6 MeV for Ca co-doping and 2.5–3.8 MeV for Sr co-doping.

This increase can be precisely gauged by the highest alpha peak, which is from the decay of ^{215}Po in the ^{227}Ac decay chain, which emits an alpha with energy of 7.386 MeV [8]. The GEE of the ^{215}Po α peak is shifted from 2.63 MeV in Ce only LaBr_3 to 3.51 MeV in Ca co-doped $\text{LaBr}_3:\text{Ce}$ and to 3.72 MeV in Sr co-doped $\text{LaBr}_3:\text{Ce}$. In other words, the alpha-to-beta ratio of $\text{LaBr}_3:\text{Ce}$ is increased by 33.5% by Ca co-doping and 41.4% by Sr co-doping.

Heavy charged particles are known to produce high dE/dx . Increased scintillation light yield for heavy charged particles indicates reduced non-linear quenching at high excitation density, which is associated with improved non-proportionality [14], [15]. It has been shown that the non-proportionality of $\text{LaBr}_3:\text{Ce}$, especially its low energy response, is improved by Ca and Sr co-doping [4]. Improved alpha GEE agrees well with this conclusion.

B. Pulse Shape Analysis

A pulse shape discrimination (PSD) technique was used to determine if the changes in GEE for α events are also associated with changes in their pulse shapes. We used a Fourier transform based PSD algorithm to extract the pulse shape information for each individual pulse. The PSD ratio (a.k.a. pulse shape descriptor) is defined by the ratio of the amplitude of the principal frequency component (DC component) to the amplitude sum of all frequency components of the transformed Fourier spectrum. A large PSD ratio roughly corresponds to a slow pulse. This method is inherently insensitive to noise and the jitter of pulse trigger due to pulse height variation, which is one of the major uncertainty contributors for PSD algorithms based on the selection of precise time windows (e.g., charge comparison).

Figs. 2–4 present the PSD results for all three crystals. Fig. 2(a) shows the PSD scatter density plot for Ce only LaBr_3 . Note that the α region (the three “islands” between 1.7 and 2.7 MeV) is slightly shifted above the γ (and β) region in terms of PSD ratio. This indicates that even in Ce only LaBr_3 , there is a pulse shape difference between α and γ pulses. A similar feature was previously observed but was too small to be useful [2]. A PSD Figure of Merit (FoM) can be used to quantify the quality of discrimination between α and γ . The FoM is commonly defined as

$$FoM = \frac{H_1 - H_2}{FWHM_1 + FWHM_2} [16].$$

H_1 and H_2 are centroids of the Gaussian fitted peaks on a pulse shape spectrum. $FWHM_1$ and $FWHM_2$ are the full-width-half-

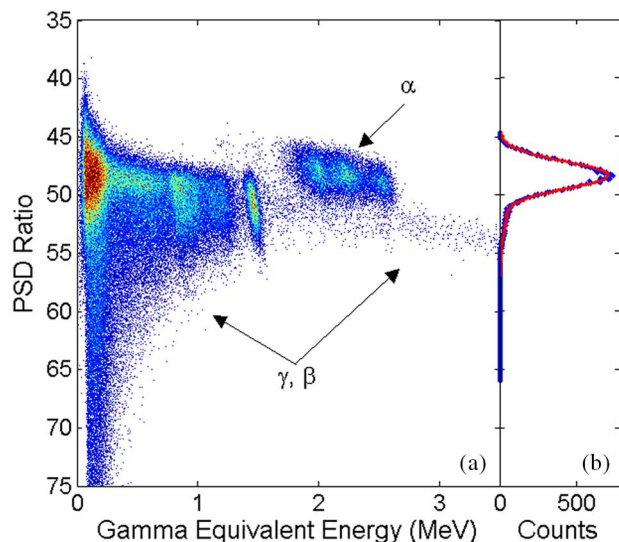


Fig. 2. (a) PSD scatter density plot of $\text{LaBr}_3:\text{Ce}$ radiation background. (b) PSD spectrum of α and γ events in the energy window 1.6–4 MeV.

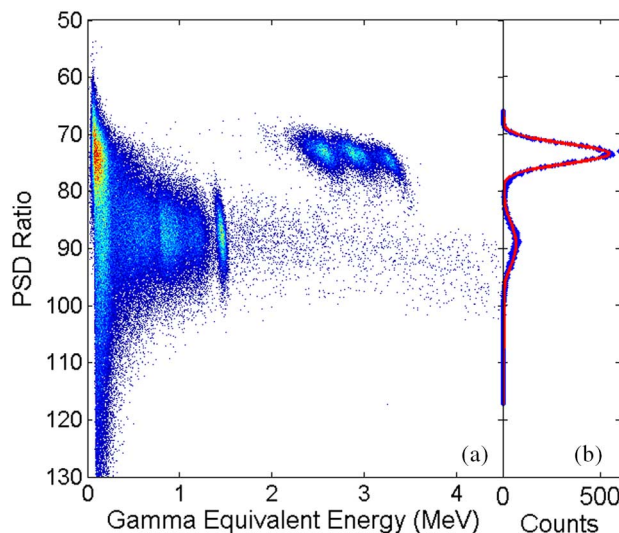


Fig. 3. (a) PSD scatter density plot of $\text{LaBr}_3:\text{Ce}$, Ca radiation background. (b) PSD spectrum of α and γ events in the energy window 1.6–4 MeV.

maximum of each Gaussian fitting. Larger FoM value corresponds to better PSD performance. In order to determine the uncertainty of the FoM, we calculated the uncertainties of all Gaussian fitting parameters (H_1 , H_2 , FWHM_1 , and FWHM_2). We then propagate their uncertainties to derive the uncertainty of the FoM according to its definition.

In the case of $\text{LaBr}_3:\text{Ce}$, the FOM is calculated to be 0.73 ± 0.04 with energy thresholds set between 1.6 MeV and 4 MeV. This PSD FoM is too low for practical application.

However, both Ca and Sr co-doped LaBr_3 crystals show significantly improved PSD performance. As is shown in Figs. 3 and 4, in addition to the increased GEE, the α events in both co-doped LaBr_3 crystals are more clearly separated from the γ events. With the same energy thresholds, the PSD FoM is determined to be 1.25 ± 0.07 for $\text{LaBr}_3:\text{Ce}$, Ca and 1.57 ± 0.03 for $\text{LaBr}_3:\text{Ce}$, Sr. With $\text{FoM} > 1.5$, complete separation can be achieved [17].

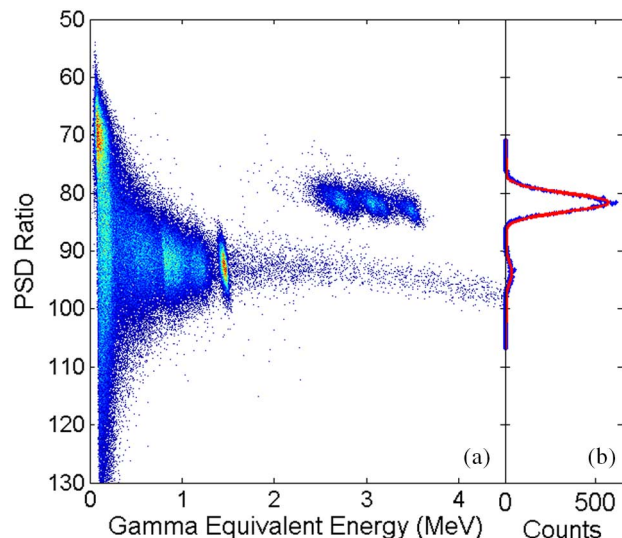


Fig. 4. (a) PSD scatter density plot of $\text{LaBr}_3:\text{Ce}$, Sr radiation background. (b) PSD spectrum of α and γ events in the energy window 1.6–4 MeV.

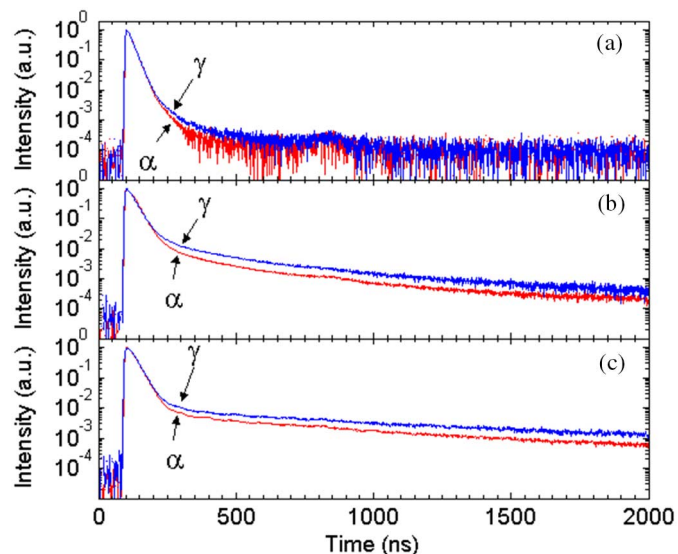


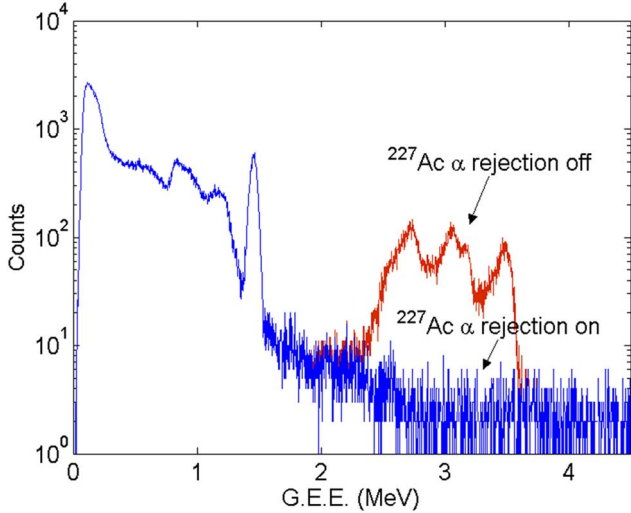
Fig. 5. Averaged PMT pulses of (a) $\text{LaBr}_3:\text{Ce}$, (b) $\text{LaBr}_3:\text{Ce,Ca}$, and (c) $\text{LaBr}_3:\text{Ce,Sr}$.

By normalizing and averaging all the α and γ pulses within corresponding energy ranges on the PSD scatter density plot, the detailed pulse shape differences can be resolved. Fig. 5 illustrates the pulse shape differences between α pulses and γ pulses for all three crystals. Even for the Ce only LaBr_3 (Fig. 5(a)), the γ pulse appears to have a very small amount of slow decay component, which makes it last slightly longer than the α pulse. The slow decay component has much stronger presence in both Ca and Sr co-doped $\text{LaBr}_3:\text{Ce}$ than the Ce only LaBr_3 .

As is shown in Fig. 5(b) and (c), the differences between α and γ pulses of co-doped crystals are much more prominent than that of the Ce only crystal. The α pulses show significantly less slow decay component than the γ pulses. This difference serves as the basis for enhanced PSD. Table II compares the percentage of light in slow decay component for all three crystals.

TABLE II
 PERCENTAGE OF LIGHT IN SLOW DECAY COMPONENT

| Particle Type | Ce only | Ce + Ca co-doped | Ce + Sr co-doped |
|---------------|---------|------------------|------------------|
| α | 1.2% | 6.3% | 9.5% |
| γ | 2.1% | 12.7% | 15.1% |

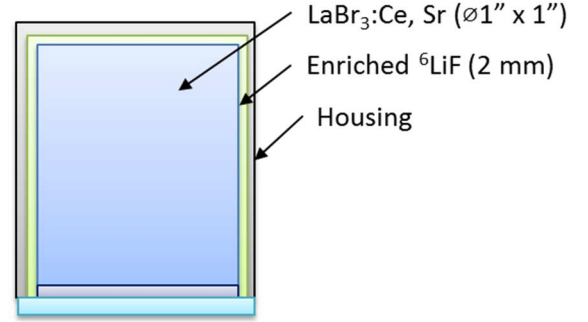

 Fig. 6. Radiation background spectrum of $\text{LaBr}_3:\text{Ce}, \text{Sr}$ with and without α rejection.

C. Background Suppression

Although rejection of internal γ and β radiations from ^{138}La is not yet possible, it is now feasible to completely eliminate the α background from co-doped $\text{LaBr}_3:\text{Ce}$. Fig. 6 illustrates the background spectra of Sr co-doped $\text{LaBr}_3:\text{Ce}$ with and without α rejection. Based on the fact that the α - γ FoM is 1.57 ± 0.03 , the rejection ratio is estimated to be 10^{-8} . With α rejection, the crystal is even able to resolve the weak 2.615 MeV γ ray from ^{232}Th in the surrounding environment. It is worth noting that the α background count rate in LaBr_3 is relatively low (0.027 counts/s/cm³ [18]) when compared to the processing speed of modern digital MCAs. The additional detector dead time introduced by α rejection should be negligible. Digital PSD processing has already been shown to work in real-time with no detrimental increase in dead-time using a fast FPGA [19]. It is also worth noting that, in Sr co-doped crystals, the lowest GEE for ^{227}Ac α 's is increased from 1.7 MeV to 2.5 MeV, which could be eliminated by a simple energy cut for certain applications.

D. Neutron-Gamma Dual Detection

Since co-doped $\text{LaBr}_3:\text{Ce}$ is able to discriminate heavy charged particles from γ photons, it is possible to construct a thermal neutron-gamma dual detector by utilizing this new feature. If co-doped $\text{LaBr}_3:\text{Ce}$ is placed in the vicinity of a neutron converter material like ^6Li , it should be able to detect and discriminate the heavy charged particles emitted by ^6Li neutron capture. The neutron capture reaction on ^6Li emits a triton with 2.75 MeV and an α particle with 2.05 MeV energy:


 Fig. 7. Schematic drawing of $\text{LaBr}_3(\text{Ce}, \text{Sr})\text{-}^6\text{LiF}$ neutron detector.

Similar to the internal α particles from ^{227}Ac decay chain, Sr co-doped $\text{LaBr}_3:\text{Ce}$ should be able to differentiate both triton and α particle from γ photons.

A prototype detector was constructed by surrounding a $(\phi 1'' \times 1'')$ Sr co-doped $\text{LaBr}_3:\text{Ce}$ crystal with 93.5% enriched ^6LiF powder. A schematic drawing is shown in Fig. 7. ^6LiF powder was used as both a neutron sensing layer and a light reflector. The energy resolution of this particular prototype detector is 2.8% at 662 keV. No degradation of γ response is observed due to the excellent reflectivity of LiF powder.

The thickness of the ^6LiF powder layers in this prototype detector is approximately 2 mm, which is much thicker than the range of tritons and α particles in LiF. Based on MCNPX 2.6 simulations, the range for a 2.75 MeV triton in LiF solid is $\sim 28 \mu\text{m}$ and the range for a 2.05 MeV α particle in LiF solid is $\sim 7 \mu\text{m}$. Even though the density of LiF powder is estimated to be 40% of the density of the solid, tritons and alphas originating near the outer surface of ^6LiF layer will lose most of their energies before reaching the LaBr_3 crystal. Effectively, only charged particles born within a few tens of microns from the LaBr_3 surface will be able to deposit energy and produce scintillation in the crystal. The proofing effect from the outer LiF powder layer further reduces the neutron detection efficiency of this detector. This detector was constructed to show proof-of-concept and was not an attempt to create the most efficient neutron detector possible.

The PSD scatter density plot for the neutron measurement is shown in Fig. 8. The same Fourier transform based PSD algorithm described in Section III-B was used for this pulse shape analysis. Similar to the previous PSD scatter density plots, the γ pulses form a “band” which spans the entire recorded energy range. The “ γ band” is not completely parallel to the x-axis but “bends” downward slightly at high energies. This is believed to result from current saturation in the PMT. Two neutron related features can be observed in the scatter plot. One is the parallelogram-shaped region between 1 and 2 MeV GEE. The other one is the region between 60 and 80 PSD ratio and 0.5 and 1 MeV GEE. The first group of events corresponds to the tritons from thermal neutron reactions with ^6Li . The second group of events is from the α particles created by the same reaction.

As is shown in Fig. 8, the neutron signals (i.e., triton signals) can be clearly separated from the γ signal with a valley in between. However, signals of α particles from $^6\text{Li}(n, t)\alpha$ are more difficult to be discriminated from γ signals mainly due to their lower GEE.

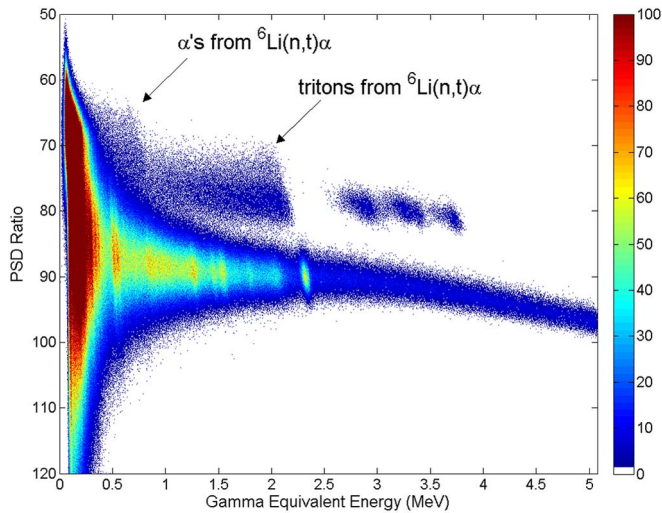


Fig. 8. PSD scatter plot for $\text{LaBr}_3(\text{Ce, Sr}) - \text{LiF}$ detector excited by ^{252}Cf .

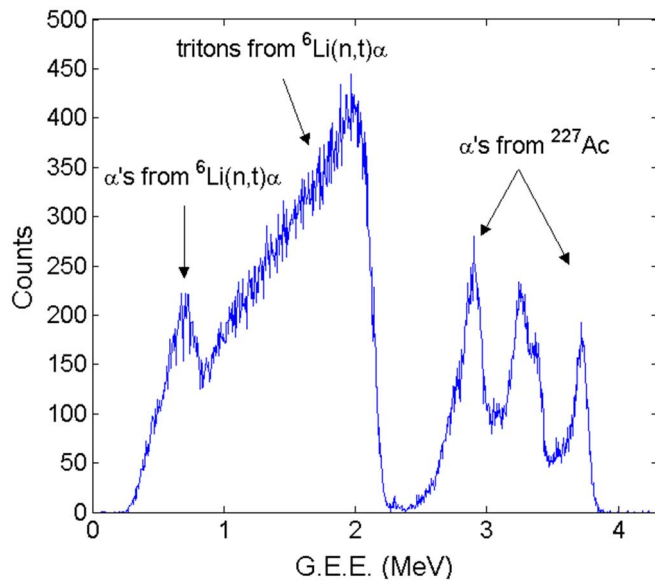


Fig. 9. Pulse height spectrum for heavy charged particles from $^6\text{Li}(n, t)\alpha$ reaction. Plot is created from Fig. 8 by energy binning the scatter points above the γ band and projecting them to the abscissa.

It is possible to create a pulse height spectrum of all heavy charged particles by separating them at the upper contour curve of the γ band. It should be noted that the counts of α events at low energies is underestimated because large portion of them are indistinguishable from γ events. Fig. 9 shows such a spectrum. The endpoint GEE for α particles is near 0.9 MeV, which corresponds to the full energy α particle at 2.05 MeV from $^6\text{Li}(n, t)\alpha$. It does not appear to be feasible to use the α signal alone as a neutron indicator due to its significant overlap with γ signals. The triton peak shows an endpoint GEE near 2.1 MeV, which corresponds to the full energy triton at 2.75 MeV.

It is worth noting that the light output for both α and triton excitation is significantly lower than the light output under γ excitation. Strong quenching is associated with both α and triton excitation. However, because tritons are more difficult to be stopped than α 's due to their lower charge-to-mass ratio, tritons effectively produce a smaller dE/dx in the crystal, which leads to less non-linear quenching. The alpha-to-beta ratio for α 's is

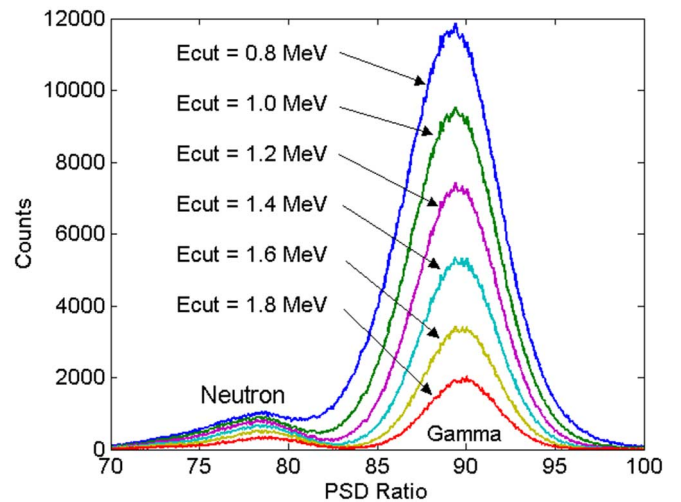


Fig. 10. Neutron-gamma PSD spectra for $\text{LaBr}_3(\text{Ce, Sr}) - ^9\text{LiF}$ detector with different lower energy thresholds.

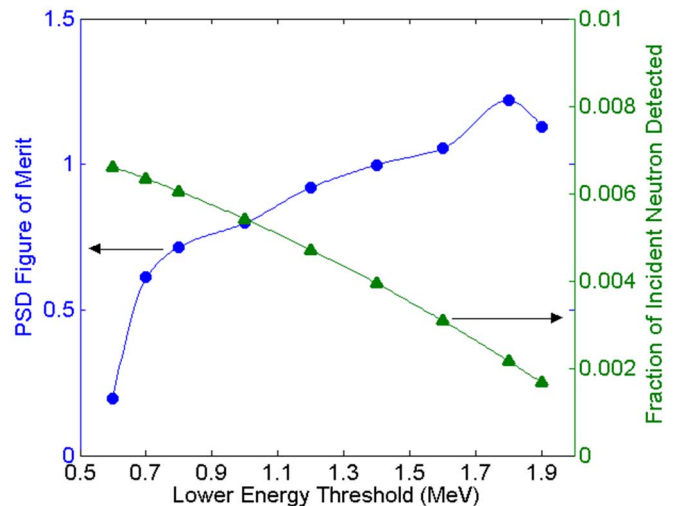


Fig. 11. Comparison of PSD Figure-of-Merit and simulated thermal neutron detection efficiency at different energy thresholds.

~ 0.45 at 2.05 MeV while the same ratio for tritons is ~ 0.76 at 2.75 MeV. Because of triton's well-positioned GEE, it is feasible to use the triton signal alone for neutron detection.

As expected, strong energy straggling is observed in the pulse height spectrum. The full energy triton peak has a large "shoulder" area toward the low energy side. In order to estimate the FoM for n- γ PSD, we set the upper energy threshold at 2.2 MeV to exclude the ^{227}Ac α background. We then varied the lower energy threshold. The PSD spectra at different energy cuts are shown in Fig. 10. A clear separation can be resolved between the neutron and gamma PSD peaks when the lower energy threshold is higher than 1.2 MeV.

Fig. 11 compares the FoM and simulated thermal neutron detection efficiency at different energy thresholds. Thermal neutron detection efficiency is defined as the fraction of incident thermal neutrons whose GEE in the LaBr_3 crystal is larger than the lower energy threshold. The highest PSD FoM is 1.22 ± 0.06 which is obtained by setting the lower energy threshold at 1.8 MeV. Due to the significant energy straggling, there is a strong degradation of detection efficiency as the

lower energy threshold is increased. Reducing the thickness of ${}^6\text{LiF}$ layer will reduce straggling, which will increase the population of full energy triton signals and eventually improve the detection efficiency with higher FoM.

It is worth noting that ${}^{139}\text{La}$ can capture a thermal neutron and undergo the following reaction: ${}^{139}\text{La}(n, \gamma){}^{140}\text{La}$. This reaction has a thermal neutron cross-section of 9 barns [20]. The reaction product ${}^{140}\text{La}$ then undergoes β^- decay and can produce a series of gamma-rays, x-rays and beta particles [21]. In a high neutron flux environment, these events may increase gamma and beta background but should be easily discriminated from the triton signals from ${}^6\text{Li}(n, t)\alpha$ by PSD. On the other hand, the shielding effect from ${}^{139}\text{La}$ should also be taken into account for large crystal detectors. For the above-described detector, ${}^{139}\text{La}$ absorbs 18% of incident thermal neutrons while ${}^6\text{Li}$ absorbs 80% based on our MCNPX simulations. A useful detector would minimize the LaBr_3 areal density and optimize the ${}^6\text{LiF}$ thickness for efficient neutron detection.

IV. CONCLUSION

Both Ca and Sr co-doping increase the GEE for heavy charged particles in $\text{LaBr}_3:\text{Ce}$. Pulse shape discrimination between α particles and γ ray photons is also significantly enhanced by co-doping. Based on this new feature, α background (between 1.7 and 2.7 MeV GEE) from ${}^{227}\text{Ac}$ can now be completely eliminated by PSD technique. This feature makes it possible to use co-doped $\text{LaBr}_3:\text{Ce}$ in certain applications whose signature energies could be masked by the ${}^{227}\text{Ac}$ background. An example of such an application is identification and abundance analysis of Si, S, and Mg in well-logging neutron capture and inelastic scattering measurements whose signatures lie in this energy range [22]. Furthermore, since the ${}^{227}\text{Ac}$ background scales with volume, its removal makes the use of larger LaBr_3 crystals more attractive.

With a ${}^6\text{LiF}$ conversion layer, Sr co-doped $\text{LaBr}_3:\text{Ce}$ can be a high-performance dual mode detector for both neutrons and gammas. Due to the very high γ - ray energy resolution of Sr co-doped $\text{LaBr}_3:\text{Ce}$, this detector configuration can be an attractive alternative to other dual mode solutions as $\text{Cs}_2\text{LiYCl}_6:\text{Ce}$ [23], $\text{Cs}_2\text{LiLaBr}_6:\text{Ce}$ [24], [25], LiF-ZnS coated bismuth-loaded plastic [26] and HgI_2 [27]. However, the neutron detection efficiency of a conversion type neutron detector is determined by the thickness of the conversion layer, which is limited by the range of neutron reaction products [28]. The efficiency of a detector with a single conversion layer can be low compared to a monolithic crystal detector. Thus, it is paramount to optimize the thickness of the ${}^6\text{LiF}$ layer and the geometry of $\text{LaBr}_3:\text{Ce}$ in order to achieve adequate neutron detection efficiency. The excellent reflectivity of LiF powder combined with the PSD enabling Sr co-dopant provides neutron detection ability to an already excellent γ -ray scintillator.

REFERENCES

- [1] E. van Loef, P. Dorenbos, and C. van Eijk *et al.*, "High-energy-resolution scintillator: Ce^{3+} activated LaBr_3 ," *Appl. Phys. Lett.*, vol. 79, pp. 1573–1575, 2001.
- [2] C. Hoel, L. G. Sobotka, and K. S. Shah *et al.*, "Pulse-shape discrimination of La halide scintillators," *Nucl. Instrum. Meth. A*, vol. 540, pp. 205–208, 2005.
- [3] K. Yang, P. R. Menge, and J. Buzniak *et al.*, "Performance improvement of large Sr^{2+} and Ba^{2+} co-doped $\text{LaBr}_3:\text{Ce}^{3+}$ scintillation crystals," in *Proc. IEEE Nuclear Science Symp. Medical Imaging Conf. (NSS/MIC)*, 2012, pp. 308–311.
- [4] M. S. Alekhin, J. de Haas, and I. V. Khodyuk *et al.*, "Improvement of γ -ray energy resolution of $\text{LaBr}_3:\text{Ce}^{3+}$ scintillation detectors by Sr^{2+} and Ca^{2+} co-doping," *Appl. Phys. Lett.*, vol. 102, p. 161915, 2013.
- [5] D. Aberg, B. Sadigh, and A. Schleife *et al.*, "Origin of resolution enhancement by co-doping of scintillators: Insight from electronic structure calculations," *Appl. Phys. Lett.*, vol. 104, p. 211908, 2014.
- [6] P. Erhart, B. Sadigh, and A. Schleife *et al.*, "First-principles study of codoping in lanthanum bromide," *Phys. Rev. B*, vol. 91, p. 165206, 2015.
- [7] M. S. Alekhin, D. A. Biner, and K. W. Kramer *et al.*, "Improvement of $\text{LaBr}_3:5\%\text{Ce}$ scintillation properties by Li^+ , Na^+ , Mg^{2+} , Ca^{2+} , Sr^{2+} , and Ba^{2+} co-doping," *J. Appl. Phys.*, vol. 113, p. 224904, 2013.
- [8] B. D. Milbrath, R. C. Runkle, and T. W. Hossbach *et al.*, "Characterization of alpha contamination in lanthanum trichloride scintillators using coincidence measurements," *Nucl. Instrum. Meth. A*, vol. 547, pp. 504–510, 2005.
- [9] P. R. Menge, G. Gautier, and A. Iltis *et al.*, "Performance of large lanthanum bromide scintillators," *Nucl. Instrum. Meth. A*, vol. 579, pp. 6–10, 2007.
- [10] L. P. Ekstrom and R. B. Firestone, WWW Table of Radioactive Isotopes, database version Feb. 28, 1999 [Online]. Available: <http://ie.lbl.gov/toi/index.htm>
- [11] B. D. Milbrath, J. I. McIntyre, and R. C. Runkle *et al.*, "Contamination studies of $\text{LaCl}_3:\text{Ce}$ scintillators," *IEEE Trans. Nucl. Sci.*, vol. 53, no. 5, pp. 3031–3034, Oct. 2006.
- [12] F. Quarati, I. V. Khodyuk, and C. van Eijk *et al.*, "Study of ${}^{138}\text{La}$ radioactive decays using LaBr_3 scintillators," *Nucl. Instrum. Meth. A*, vol. 683, pp. 46–52, 2012.
- [13] "Gamma-ray spectrum catalogue, Ge and Si detector spectra 4th edition," Idaho National Engineering & Environmental Laboratory 1999.
- [14] R. B. Murray and A. Meyer, "Scintillation response of activated inorganic crystals to various charged particles," *Phys. Rev.*, vol. 122, no. 3, p. 815, 1961.
- [15] R. T. Williams, J. Q. Grim, and Q. Li *et al.*, "Excitation density, diffusion-drift, and proportionality in scintillators," *Phys. Status Solidi B*, vol. 248, no. 2, pp. 426–438, 2011.
- [16] K. Yang and P. R. Menge, "Pulse shape discrimination of $\text{Cs}_2\text{LiYCl}_6:\text{Ce}^{3+}$ scintillator from -30°C to 180°C ," *Nucl. Instrum. Meth. Phys. Res. A*, vol. 784, pp. 74–79, 2015.
- [17] R. A. Winyard, J. E. Lutkin, and G. W. McBeth, "Pulse shape discrimination in inorganic and organic scintillators. I," *Nucl. Instrum. Meth.*, vol. 95, no. 1, pp. 141–153, 1971.
- [18] F. Quarati, P. Dorenbos, and J. van der Biezen *et al.*, "Scintillation and detection characteristics of high-sensitivity CeBr_3 gamma-ray spectrometers," *Nucl. Instrum. Meth. Phys. Res. A*, vol. 729, pp. 596–604, 2013.
- [19] Bridgeport Instruments, eMorpho MCA datasheet [Online]. Available: <http://www.bridgeportinstruments.com>
- [20] M. B. Chadwick, M. W. Herman, and P. Obložinsky *et al.*, "ENDF/B-VII.1. Nuclear data for science and technology: Cross sections, covariances, fission product yields and decay data," *Nucl. Data Sheets*, vol. 112, p. 2887, 2011.
- [21] NuDat 2.6, National Nuclear Data Center 2011, Brookhaven National Laboratory [Online]. Available: <http://www.nndc.bnl.gov/>
- [22] C. Stoller, B. Adolph, and M. Berheide *et al.*, "Use of LaBr_3 for down-hole spectroscopic applications," in *Proc. IEEE Nuclear Science Symp. Medical Imaging Conf. (NSS/MIC)*, 2011, pp. 191–195.
- [23] J. Glodo, W. M. Higgins, and E. van Loef *et al.*, "Scintillation properties of 1 inch $\text{Cs}_2\text{LiYCl}_6:\text{Ce}$ crystals," *IEEE Trans. Nucl. Sci.*, vol. 55, no. 3, pp. 1206–1209, Jun. 2008.
- [24] J. Glodo, E. van Loef, and R. Hawrami *et al.*, "Selected properties of $\text{Cs}_2\text{LiYCl}_6$, $\text{Cs}_2\text{LiLaCl}_6$, and $\text{Cs}_2\text{LiLaBr}_6$ scintillators," *IEEE Trans. Nucl. Sci.*, vol. 58, no. 1, pp. 333–338, Feb. 2011.
- [25] K. Yang, P. R. Menge, and J. Lejay *et al.*, "Scintillation properties and temperature responses of $\text{Cs}_2\text{LiLaBr}_6:\text{Ce}^{3+}$," in *Proc. IEEE Nuclear Science Symp. Medical Imaging Conf. (NSS/MIC)*, 2013, pp. 1–6.
- [26] N. J. Cherepy, R. D. Sanner, and P. R. Beck *et al.*, "Bismuth- and lithium-loaded plastic scintillators for gamma and neutron detection," *Nucl. Instrum. Meth. Phys. Res. A*, vol. 778, pp. 126–132, 2015.
- [27] Z. W. Bell, K. R. Pohl, and L. van den Berg, "Neutron detection with mercuric iodide," *IEEE Trans. Nucl. Sci.*, vol. 51, no. 3, pp. 1163–1165, Jun. 2004.
- [28] D. S. McGregor, M. D. Hammig, and Y.-H. Yang *et al.*, "Design considerations for thin film coated semiconductor thermal neutron detectors—I: basics regarding alpha particle emitting neutron reactive films," *Nucl. Instrum. Meth. Phys. Res. A*, vol. 500, pp. 272–308, 2003.